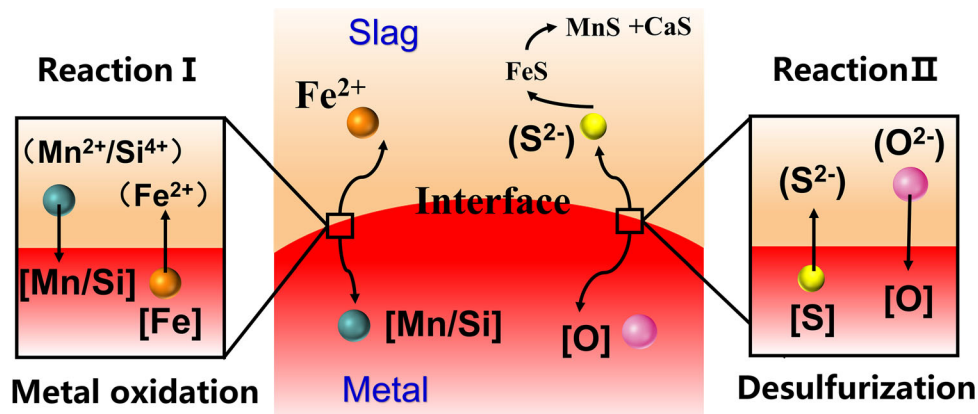# Insights into Interfacial Structure of Slag–Metal Interface During Desulfurization Through XPS and DFT Simulations

XIAOBO HE and LIJUN WANG

Ultra-low sulfur steel has excellent resistance to pitting and hydrogen-induced cracking, and is mainly used for gas pipeline steel, drilling steel and steel for structural parts of offshore platforms. This study reveals the limiting aspects of desulfurization at slag–metal interface from the perspective of experimental and theoretical calculations. Based on XPS results, the quantitative analysis shows that the relative contents of Si and O are decreasing and that of Ca, Mn and S are increasing as the etching depth increases at the slag–metal interface. Mn exists mainly as a divalent (Mn^{2+}), S exists as a negative divalent (S^{2-}), and Fe exists as a Fe–O and Fe–S at the same time. Under the conditions in this study, the analysis shows that the slag–metal interface is mainly composed of bridged oxygen (BO) and non-bridged oxygen (NBO), and the content of BO gradually decreases and that of NBO gradually increases as the depth deepens. With increasing basicity, the interfacial bridged oxygen gradually decreases and the NBO gradually increases. The increase in basicity leads to faster diffusion of sulfur and therefore to a decrease in Fe–S at the interface. Based on the experiment and simulation results, in this system, two main exchange reactions occur at the slag–metal interface, one is the exchange reaction between Fe and Mn/Si, and the other is the exchange of sulfur with oxygen. Afterwards, the Sulfur enters the slag and forms stable sulfides with Ca/Mn at the interface.

XIAOBO HE is with the Collaborative Innovation Center of Steel Technology, University of Science and Technology Beijing, Beijing 100083, P.R. China and also with the State Key Laboratory of Advanced Metallurgy, University of Science and Technology Beijing, Beijing 100083, P.R. China. Contact e-mail: lijunwang@ustb.edu.cn LIJUN WANG is with the Collaborative Innovation Center of Steel Technology, University of Science and Technology Beijing.

I. INTRODUCTION

SOCIO-ECONOMIC development has put forward higher standards for the performance of steel and high-grade pipeline steels, offshore platform steels, pressure vessel steels, high-quality electrical steels and bearing steels have extremely high requirements for sulfur content.[1] Understanding the desulfurization mechanism and dynamics of the interaction between

metal and slag phases in high-temperature processes can help improve desulfurization efficiency and product quality.[2,3] During the whole process sulfur first migrates from the metal phase to the slag–metal interface, followed by an interfacial chemical reaction, and finally migrates from the interface to the slag, and the actual industrial process even involves reactions at the gas interface and gas-phase mass transfer of the species involved.[4] The dissolution and removal of sulfur mainly occur at the slag–metal interface, and the interface is in dynamic change, so the distribution and migration of sulfur at the interface is the focus and difficulty of the interface research.

According to the exchange reaction equation for sulfur proposed by Richardson,[5] desulfurization is closely related to the oxygen structural unit in the slag at the interface. Previous studies[6] have shown that the slag consists of three different types of oxygen [free oxygen, non-bridged oxygen (NBO) and bridged oxygen (BO)] and the ratio of the three affects the desulfurization. Park et al.[7] gave a linear relationship between the sulfide capacity and O^{2-}. Wang et al.[8] indicated that there is a linear relationship between sulfur capacity and average oxygen in Cr-containing slags, not only free oxygen, indicating that the magnitude of sulfur capacity is closely related to the slag structure and the form of oxygen in the slag. Kang[9] showed that sulfur displaces three different types of oxygen in the slag by thermodynamic analysis, but the type and order of substitution were not investigated. Our group recently resolved the structural characteristics and charge distribution information of the simple binary silicates system based on first principles of molecular dynamics (AIMD),[10,11] elucidating the different replacement order of oxygen in the desulfurization process, and laid a reliable foundation for the later in-depth understanding of the existence and migration forms of sulfur in different systems and the explanations of desulfurization.

Despite the extreme importance of structural information, the interfacial phenomena and their structure are still not well understood due to the complexity of the slag interface, the high temperature and the various chemical compositions involved in the process, which explains the difficulty in performing proper experiments and clarifying these phenomena. Furthermore, the nature and exact mechanisms by which the interfacial structure controls the reactions of these processes are complex and not yet understood. At present, the researches on interfacial phenomena mainly focus on the surface/Interfacial tension of slag, slag–metal interfacial tension. The great efforts have been made by researchers[12–15] on measuring surface tension by digital image processing analysis based on the droplet shape and X-ray method. In addition, Coley[16,17] and Toshihiro Tanaka[18,19] studied the dynamics of interfacial phenomena and the interfacial oxygen potential based on kinetic data. However, the above studies have rarely examined the essential structure of the interface. Recently, our group has developed a novel method to study the gas-slag interfacial structure,[20,21] presenting the interface structure and element distribution. It provides a very useful tool for insight into the slag–metal interface. Meantime, advances in computational methods offer the possibility to simulate and predict slag structure and interfacial interactions.[22–25]

In present study, X-ray photoelectron spectroscopy was used to resolve and characterize the slag–metal interface structure of slag. The main objective of this work is to gain a deeper understanding of the interaction between slag and metal phases, with emphasis on the interfacial slag structure and the variation of elemental distribution with depth. Simulation studies of slag–metal interface interactions and elemental valence distributions using the AIMD method have also been carried out to lay the foundation for efficient desulfurization and slag system design.

II. METHODS

A. Experimental Methods

The samples of slag and metal in the experiment were prepared from CaO, SiO$_2$, MnO, Al$_2$O$_3$, iron powder, and distilled sulfur powder. All materials are reagent-grade samples produced by Sinopharm Corporation. CaO was obtained by sintering CaCO$_3$ at 1000 °C for 8 hours, and all other samples were dried in an oven to remove moisture. Table I listed the initial composition of slag and metal. S-A,S-B,S-C represent three different basicity slags. Mix the iron powder and sulfur powder in the agate mortar for half an hour according to the ratio in Table I, and then put them into the bottom of the alumina crucible. For the slag sample, the four oxides were mixed in the agate mortar in the proportions shown in Table I and then pressed into a cylindrical sample in the crucible.

The experimental equipment (Vertical furnaces produced by Henan Bleimant, China) and sample arrangement have been shown in Figure 1. Firstly, the crucible is placed in the bottom of the furnace tube and heated up to 1000 °C with a heating rate of 5 °C/min and then to the target temperature of 1600 °C with a heating rate of 3 °C/min. The whole process is protected by the flow rate of 400 mL/min argon gas. After that, the sample was held at 1600 °C for 30 minutes. After the experiment is completed, the crucible is quickly removed and quenched in water. Finally, the slag and Fe–S melt are separated for testing. The photo of the slag–metal separation is shown in Figure 1, the metal liquid will agglomerate into a sphere, so the slag–metal interface is arc-shaped, take a small piece of this region directly for X-ray photoelectron spectroscopy test, so as to get the information of the interface. The above steps were repeated for samples of different basicity.

The physical phases of the samples were detected by an X-ray diffractometer (the Dutch brand PANalytical X 'Pert). The bulk structure was subjected to Raman testing (HORIBA Scientific LabRAM HR Evolution) and XRF (PANalytical Axios). The high-resolution spectra of Fe, Mn, O and S elements at the slag–metal interface were detected using X-ray photoelectron spectroscopy (Thermo Fisher ESCALAB 250Xi). The XPS device used is an X-ray source with an aluminum target

Table I. The Initial Composition of Slag and Metal (Wt Pct)

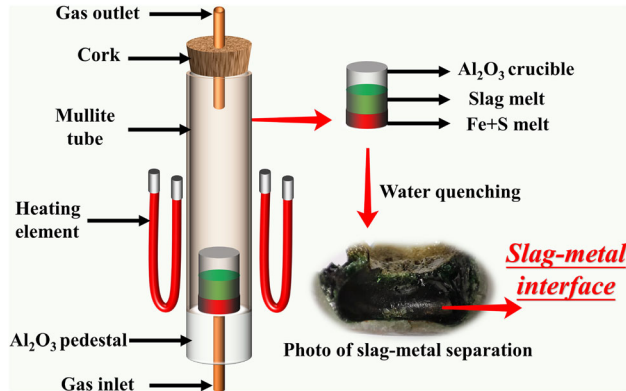|	CaO	SiO$_2$	MnO	Al$_2$O$_3$	Fe	S	B
Slag-A(S-A)	28.33	56.67	5	10	—	—	0.5
Slag-B(S-B)	37.78	47.22	5	10	—	—	0.8
Slag-C(S-C)	46.36	38.64	5	10	—	—	1.2
Metal	—	—	—	—	99.5	0.5	—

Fig. 1—Experimental equipment diagram.

and a spot size of 500 μm. For the tests at different depths, the argon-ion etching technique was used to etch six times, with each etching lasting 60 seconds for a total of 360 seconds.

During the XPS analysis, the peaks of all elements were calibrated with peaks in the C1s (284.8 eV) orbit. Since the outer surface of the sample may be contaminated between the experiment and XPS detection, the data is processed with the analysis after 60 seconds. AVANTAGE software was used for split peak fitting of different elements and quantitative analysis of the full spectrum. All the details of the analysis are mentioned in the previous literature.[21]

B. Computational Simulation Methods

In current work, the first-principle calculation was performed in the framework of density functional theory (DFT) via Vienna ab-initio simulation package (VASP) code.[26,27] All calculations use projector augmented wave (PAW)[28] datasets supplied in the VASP-PAW package and the Perdew–Burke –Ernzerhof (PBE)[29] exchange–correlation functional. All simulations were performed in a canonical ensemble (NVT: constant number of particles, volume, and temperature), with temperature controlled by a Nosé thermostat.

Due to the fact that metal oxidation and desulfurization mainly occur at the slag–metal interface, while previous studies[21] have shown that Ca is not an interfacially active element, on the other hand, due to the limitations of first principles calculations and the lack of computing power, this study only simulates the desulfurization process of the Mn–Si–O containing system and the slag–metal interface. The initial structure

of MnSiO$_3$ was reported in the literature.[30] The lattice parameters of the solid MnSiO$_3$ are $a = 9.79$ Å, $b = 10.51$ Å, $c = 12.23$ Å, $\alpha \approx 108.5$ deg, $\beta \approx 103.2$ deg, and $\gamma \approx 82.3$ deg. Due to the need for interface modelling, MnSiO$_3$ is sectioned to give three termination layers, as O-termination layer, Mn-termination layer and Si-termination layer. Structural optimization of the three termination layers reveals that the O termination layer has the lowest energy, followed by the Mn-termination layer and the Si-termination layer, as shown in Figure 2(a). Therefore, for the calculation of the slag–metal interface, this study focuses on the O-termination layer.

For the slag–metal interface, the four sulfur atoms of the interface are replaced and the two different termination surfaces are shown in Figure 2(b). The start structure is a cubic cell of 116 atoms, including 41 Fe atoms, 20 Mn atoms, 10 Si atoms, 41 O atoms and 4 S atoms. Firstly, the system was heated to 1873 K, after which it was held at 1873 K for 5 ps with a timestep of 1.0 fs. And the last 5.0 ps was employed to extract the required properties. For charge analysis, perform charge calculation after melting the calculation result. Then the Bader charge analysis method was utilized to clarify the valence situation of the slag melt. Bader analysis result is obtained from charge density generated by first-principles DFT calculations. Charge calculation analysis using the VASPKIT[31] and VESTA.[32]

III. RESULTS AND DISCUSSIONS

A. Elemental Distribution and Present State of Sulfur and Metal Cations at the Slag–Metal Interface

Sulfur removal is mainly accomplished through exchange reactions at the slag–metal interface. It is interested to figure out how the different elements are distributed in the slag side when interacting with Fe–0.5 wt pct S melt. This section discusses the interfacial element distribution using a slag system with a basicity of 0.5 as an example. Firstly, the slag-A has confirmed the glass state by XRD analysis, as shown in Figure 3(a). The full XPS spectrum of various elements present in Figure 3(b), Sulfur has been detected in slag phase, which means the S has transferred through slag–metal interface. Figure 3(c) shows the quantitative results of the elements of Ca, Si, Al and O, except for Mn, S and Fe due to their low content in slag phase. As can be seen from Figure 3(c), with the increase of etching depth, the content of Ca keeps increasing, the content of Si keeps decreasing, and the relatively steady state is reached after 180 seconds. While the relative content of oxygen is constantly decreasing, the content of Al remains unchanged. At the same time, the composition of the bulk slag after the experiment is shown in Table II. The results show that part of the Al$_2$O$_3$ dissolved into the slag partly due to the presence of the alumina crucible. The comparison revealed some differences between the XPS interfacial quantification results and the bulk results obtained by XRF, which is since XPS is a semi-quantitative method whose main
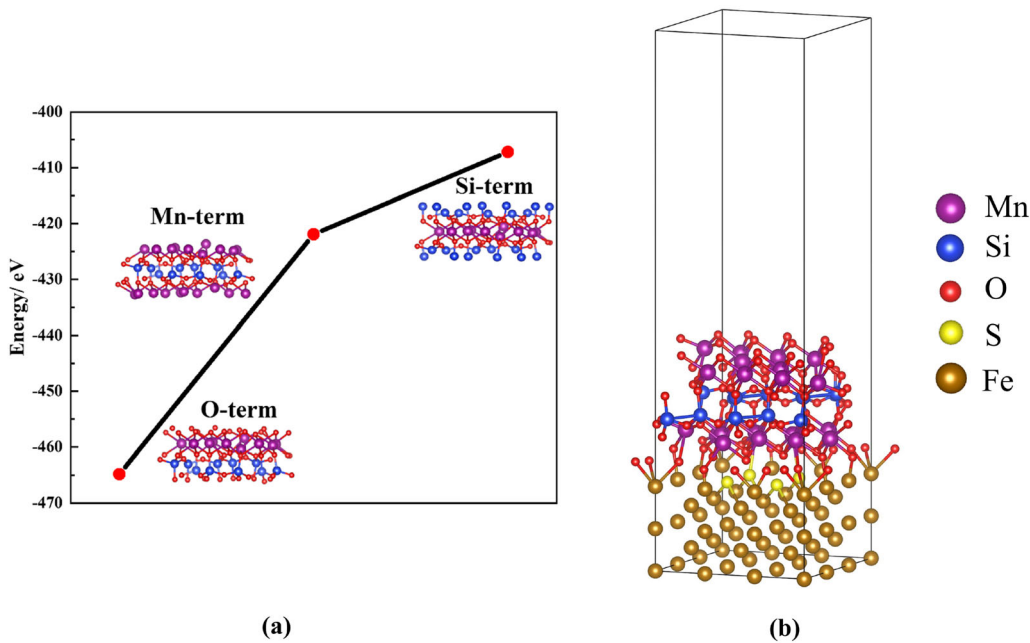
Fig. 2—(a) Energy at different termination levels; (b) O-termination layer in slag–metal interface.
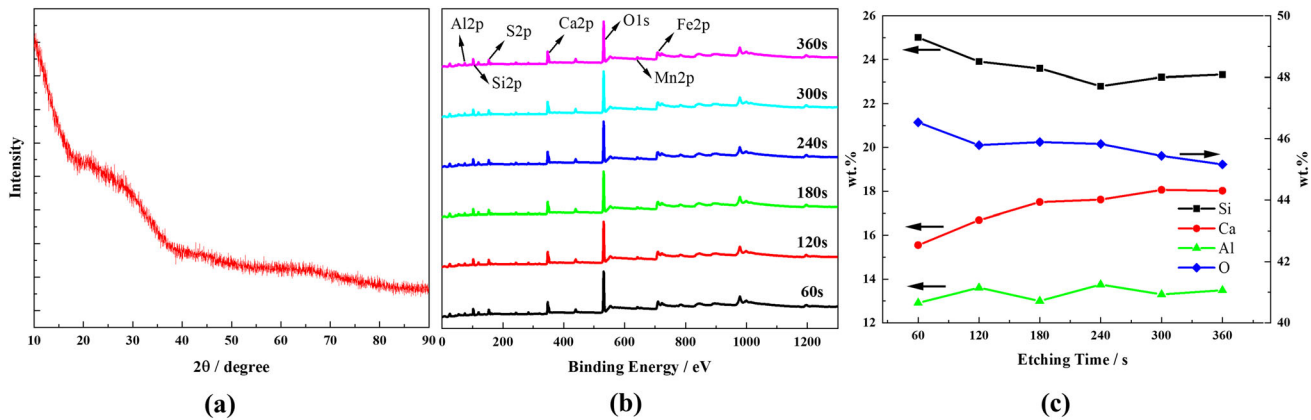

Fig. 3—(a) XRD pattern of slag-A; (b) Full spectrum for different etching time in slag-A; (c) relative content of elements in slag-A.

Table II. The Final Composition of Slag (Wt Pct)

	CaO	SiO$_2$	MnO	Al$_2$O$_3$	Fe$_x$O
Slag-A(S-A)	22.974	31.523	4.179	29.326	11.998
Slag-B(S-B)	29.366	25.91	4.137	31.828	8.759
Slag-C(S-C)	36.438	20.953	4.607	30.345	7.657

purpose is to analyze elemental valence and oxygen structure, on the other hand, since Al is not an interfacially active element, it is less present in the XPS quantification. However, in this study, the focus is on the elemental distribution pattern with depth at the slag–metal, and the elemental variation pattern obtained by XPS at different depths is accurate. Therefore, it can be obtained that the relative content of Si and O is relatively high at the slag–metal interface, which proves that the interface is dominated by highly polymerized Si–O units.

To determine the distribution of sulfur and metal cations, the peaks were analyzed for different etching time. For the quantification of trace elements, the intensity of the peaks at different etching time was analyzed. Figure 4 shows the high-resolution core spectra of S2p, Fe2p and Mn2p with different etching time. As shown in Figures 4(a) and (b), the peak intensity of S2p increases continuously from 60 to 240 seconds, while the peak intensity of sulfur slightly decreases and stabilizes after 240 seconds. Figures 4(e) and (f) show that the peak intensity of Mn2p increases gradually with the increase of etching depth, indicating that the relative content of Mn gradually increases. However, due to the existence of different valence states in the peaks of Fe2p, the relative content of Fe2p is obviously different from
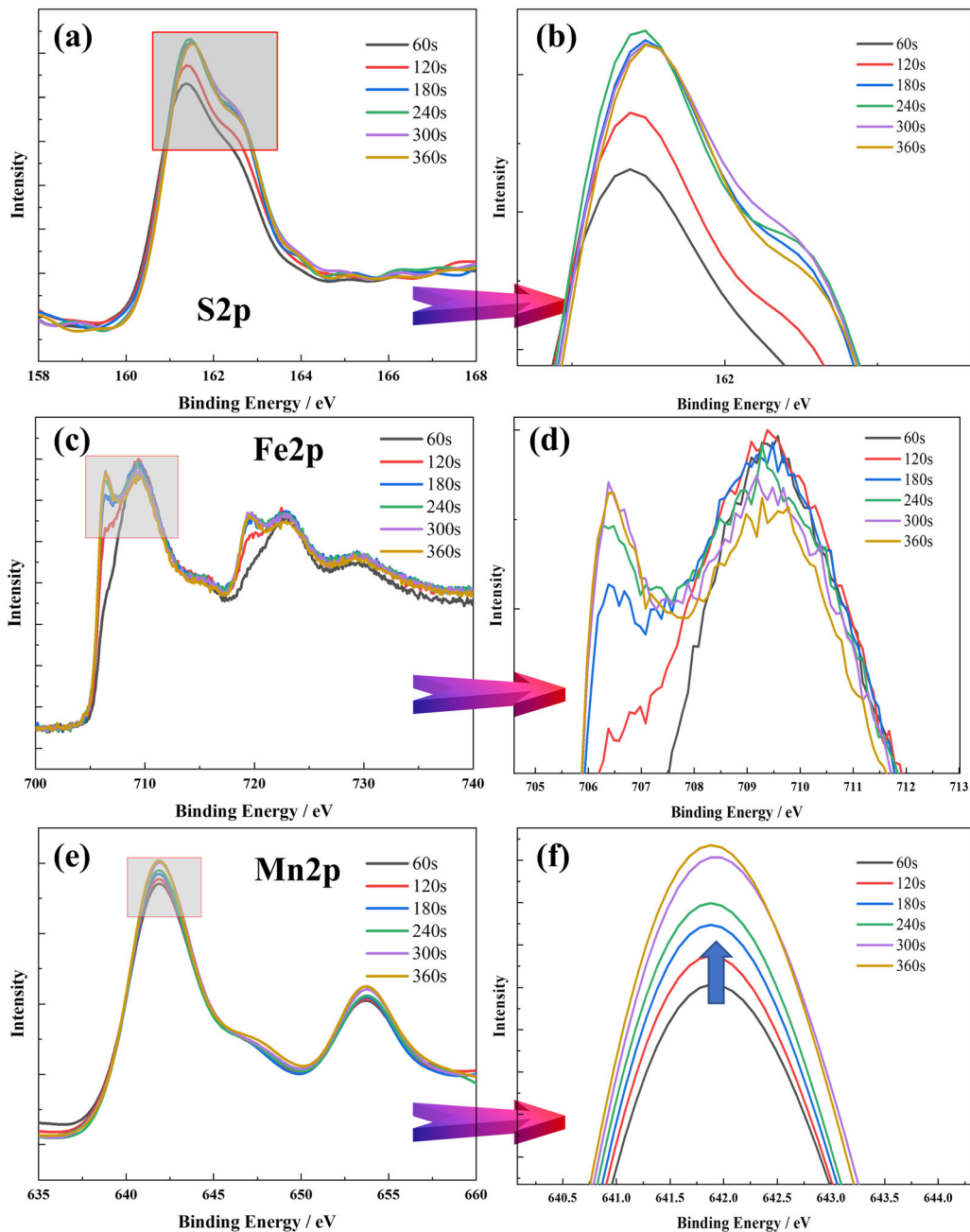
Fig. 4—XPS spectra of different etching time in slag-A: (*a*, *b*) High-resolution core-level spectra of S2p and enlarged image; (*c*, *d*) High-resolution core-level spectra of Fe2p and enlarged image; (*e*, *f*) High-resolution core-level spectra of Mn2p and enlarged image.

that of the two elements. Figures 4(c) and (d) show that the intensity of peak between 706 and 708 eV increases continuously with the etching depth, while the peak intensity does not change after etching for 300 seconds. However, the peak intensity between 708 and 712 eV decreases with increasing depth. The valence state of Fe corresponding to the two will be discussed in the following fitting analysis.

The reference XPS peaks for all elements are listed in Table III. For the Mn2p peak, the literature[33,34] shows that there are multiple split peaks, while at 641 eV there are peaks of both MnO and Mn_2O_3, as a result,

distinguishing the peaks of different valence states is difficult, whereas the Mn3s peak can be used to clearly differentiate the valence state of Mn. XPS-related literature[33,35] shows that the Mn3s peak with a difference of 6 eV between the two peaks is the MnO peak, and the one with a difference of about 5.3 eV is the Mn_2O_3 peak, while a satellite peak exists for MnO at about 647 eV, while Mn_2O_3 does not exist. Since there is only an intensity change of the peak of Mn with depth, the results of 180 seconds are analyzed and discussed. The fitting results of the Mn peak are shown in Figures 5(a) and (b), and the results show that a satellite

peak exists at 647 eV, while the difference of the Mn3s peak is 6 eV, thus indicating that Mn is mainly present in the divalent form at the slag–metal interface. For the Fe2p peaks, the peaks at 706.7 eV, 709.6 eV are Fe–S and Fe–O peaks, respectively.[34,36–38] As shown in Figure 5(d), Fe is mainly dominated by Fe–O and Fe–S, combined with Figures 4(c) and (d), with the increase of depth, the peak of Fe–S gradually enhances, while the peak of Fe–O decreases, indicating the existence of both Fe–S and Fe–O at the slag–metal interface. For the S2p peak, the literature[39–41] show that the negative divalent peak of S is in the range of 160 to 162 eV, and the tetravalent and hexavalent peaks of S are in the range of 168 to 172 eV. Figure 5(c) shows that the peak of S2p only exists as a negative divalent peak, so sulfur exists only as S^{2-} at the slag–metal interface. Based on the results of the elemental distribution, the possible reactions are further discussed.

Firstly, due to the contact between the slag and metal, the main reaction is the oxidation of the metal. The presence of Fe–O is due to the contact of the metal with the oxide slag. From the slag–metal interface reaction in Table IV, it can be obtained that MnO in the slag is more preferential for the oxidation of Fe in metal. The following two reactions may occur

$$[Fe] + Mn^{2+} = (Fe^{2+}) + [Mn] \qquad [1]$$

$$[Fe] + 1/2(Si^{4+}) = (Fe^{2+}) + 1/2[Si] \qquad [2]$$
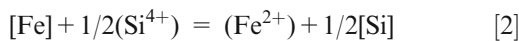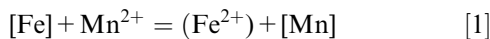
However, due to the high SiO_2 content, the main reaction that takes place at the interface is Eq. [2]. In addition to the oxidation reactions, the elemental distribution results indicate that the sulfur removal reactions occur at the interface, the main reactions are as follows

$$[S] + (O^{2-}) = [O] + (S^{2-}) \qquad [3]$$
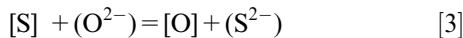
The elemental distribution indicates that sulfur has entered the slag, but that it will later form stable compounds with cations. In previous studies by our group,[10,11,42] it was shown experimentally and computationally that sulfur is present in the slag mainly around the metal cations Mn or Fe. At the same time, the cations will have an aggregation effect, thus affecting the desulfurization. The removal of sulfur is mainly related to the stability of the sulfide and the structure of the oxygen. In the slag–metal reaction, sulfur is dissolved into the molten oxide by Eq. [3] after which sulphides are formed and interconverted. As shown in Table IV, the stability of sulfides calculated by FactSage indicates that CaS is the most stable sulfide, followed by MnS and FeS. Although CaS is thermodynamically the most stable sulfide, our previous studies[10,11,42] have shown that Mn and Fe have a greater influence on sulfur uptake and dissolution due to the presence of d electrons in their transition metal elements. The literature[43,44] shows that the content of SiO_2 and Al_2O_3 affects the stability of sulfides, under low basicity conditions (high SiO_2 and Al_2O_3), FeS or MnS are more stable than CaS,

while the opposite conclusion is reached under high basicity conditions. Thus, at the interface, due to contact with the metal, sulfur will form FeS with iron and be stable, In the discussion of this manuscript, the samples have low basicity, so FeS and MnS are relatively more stable. The results show that there is relatively more Si and O at the interface, so that the basicity at the interface can be considered lower than that in the bulk. In addition, the atoms of Mn, Fe have small radius and they can aggregate at the interface, but the atoms of Ca have larger radius and do not aggregate at the interface. In summary, with the increase of depth, it can be assumed that the basicity is increasing, so the FeS at the interface will be partially converted to MnS or CaS.

For different basicity, the XPS spectra of the elements are shown in Figures S1–S4 in supplementary material. As shown in Figure S1, the spectrum of Fe2p is significantly different at 706 eV, indicating above that the peak is the Fe–S bond, and therefore the intensity of the Fe–S bond is weakening with increasing basicity, suggesting a decrease in Fe–S bonding. Figure S2 shows that the peak of Mn is not very sensitive to basicity, since the MnO content in the slag system does not change. Figure S3 shows that the peak of O1s shifts towards lower binding energies with increasing basicity, due to the increase in basicity leading to depolymerisation of the structure and as a result the interfacial structure also changes. For the sulfur peak, Figure S4 shows that the position of the peak does not change much with increasing basicity, but the signal intensity of the peak is becoming noisier, indicating a weakening of the interfacial sulfur content, which is consistent with a reduction in Fe–S bonding. The distribution of elements at this interface is due to the influence of basicity. The literature[45] shows that the higher the basicity, the higher the sulphide capacity and the higher the sulfur diffusion coefficient. Therefore the sulfur at the interface will be reduced and thus the Fe–S bond will be reduced. In the next section, further analysis is carried out in conjunction with the structure.

B. Slag–Metal Interface Structure and Sulfur Removal Mechanism

As mentioned above, the transfer of sulfur from the metal liquid to the slag phase occurs through an exchange reaction with oxygen, so the form of oxygen at the interface is critical to the absorption and dissolution of sulfur. A detailed fitting analysis of the peaks of O1s was carried out. As reported in the literature[46–48] about O1s, the peaks between 532 and 532.6 eV are BO, while the peaks between 531 and 531.5 eV are NBO peaks. Figure 6(a) shows the O1s spectrum for different etching time in slag-A, and the results show that the oxygen peak gradually migrates to the low binding energy direction with increasing depth. Figures 6(b) and (c) show a typical fit and the quantitative results in slag-A. The results show that there are mainly bridged and NBO at the slag–metal interface, the BO content is above 60 pct, while the NBO content is less than 40 pct. As the etching depth increases, the

Table III. Reference XPS Peaks of Mn, Fe, S and O

		ΔE		References
Mn3s	Mn^{2+}	6 eV	—	14,15
	Mn^{3+}	5.3 eV	—	
		position	satellite peak	
Mn2p	Mn^{2+}	641 eV	647 eV	16,17
	Mn^{3+}	641 eV	—	
Fe2p	Fe–S	706.7 eV	—	17–20
	Fe–O	709.6 eV	—	
S2p	S^{2-}	160 to 162 eV	—	21–23
	S^{4+}	166–168 eV	—	
	S^{4+}	168–170 eV	—	
O1s	free oxygen	528 eV	—	24–26
	non-bridged oxygen	531 to 531.5 eV	—	
	bridged oxygen	532 to 532.6 eV	—	
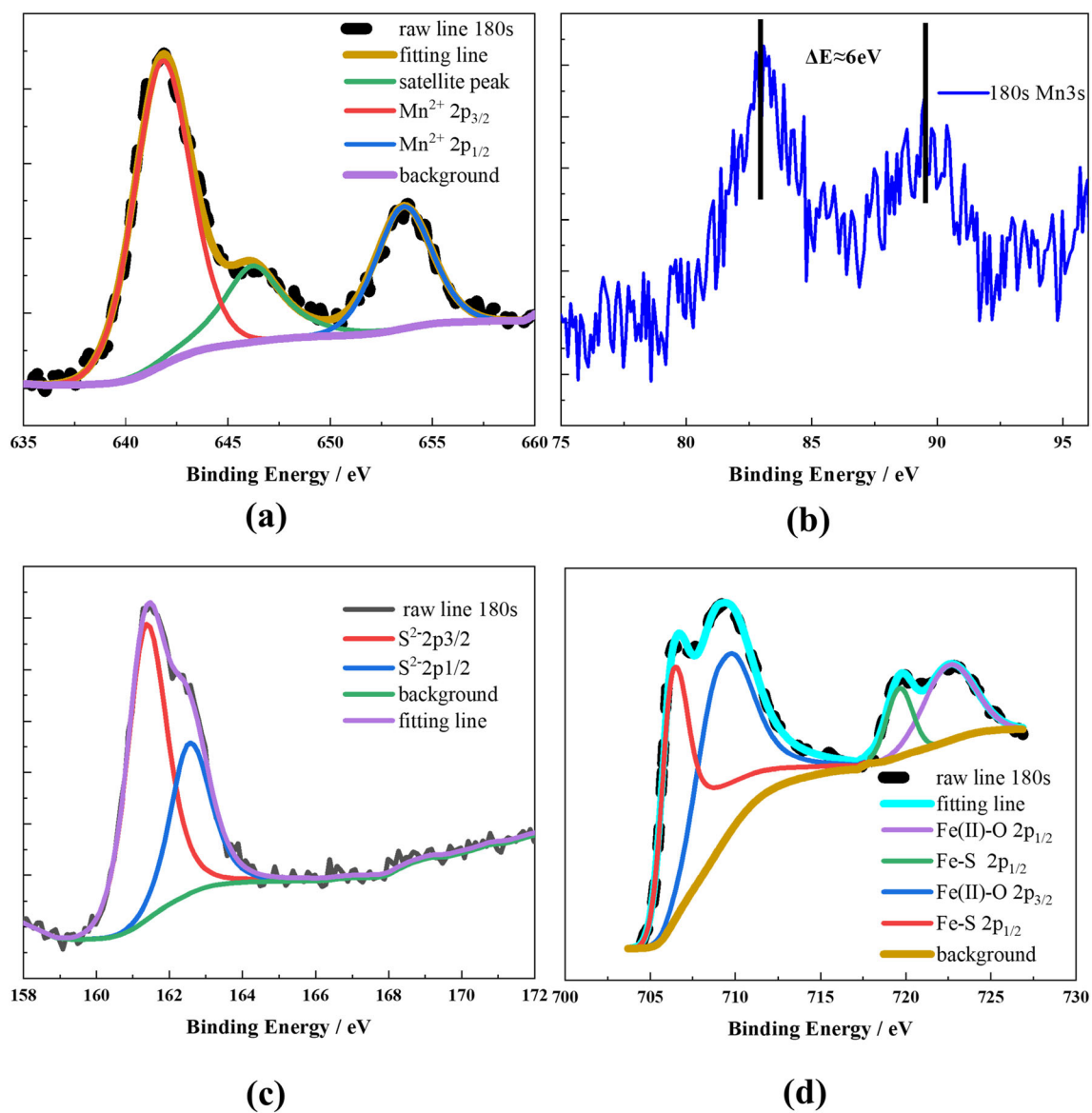
Fig. 5—Typical fitted spectra in slag-A at 180 s: (*a, b*) Mn2p and Mn3s; (*c*) S2p; (*d*) Fe2p.

proportion of BO declines whereas the that of NBO increases, and tends to form a plateau after 180 seconds. Compared with the gas-slag interface,[21,49] the slag–metal interface structure of this system has more BO and less NBO, which is partly due to the lower basicity of the slag, and partly due to the addition of 10 wt pct Al_2O_3 to

the system resulting in more BO and less NBO in the slag. At the same time, due to the presence of ferrous oxide, the oxygen potential at the slag–metal interface is higher, so there is more BO.

The results of the fit for different basicity slags are shown in Figure S5 in supplementary material. As the basicity increases, the content of BO decreases and that of NBO increases, due to the increased basicity depolymerising the slag structure. However, at basicity 0.5, equilibrium was reached after 180 seconds of etching, at basicity 0.8, equilibrium was essentially reached after 120 seconds, and at basicity 1.2, there was essentially no change in content. This suggests that the extent of the boundary layer decreases with increasing basicity, which is also consistent with the results at the gas-slag interface.[49]

Table IV. The $\Delta G°$ for Different Reactions at 1873 K

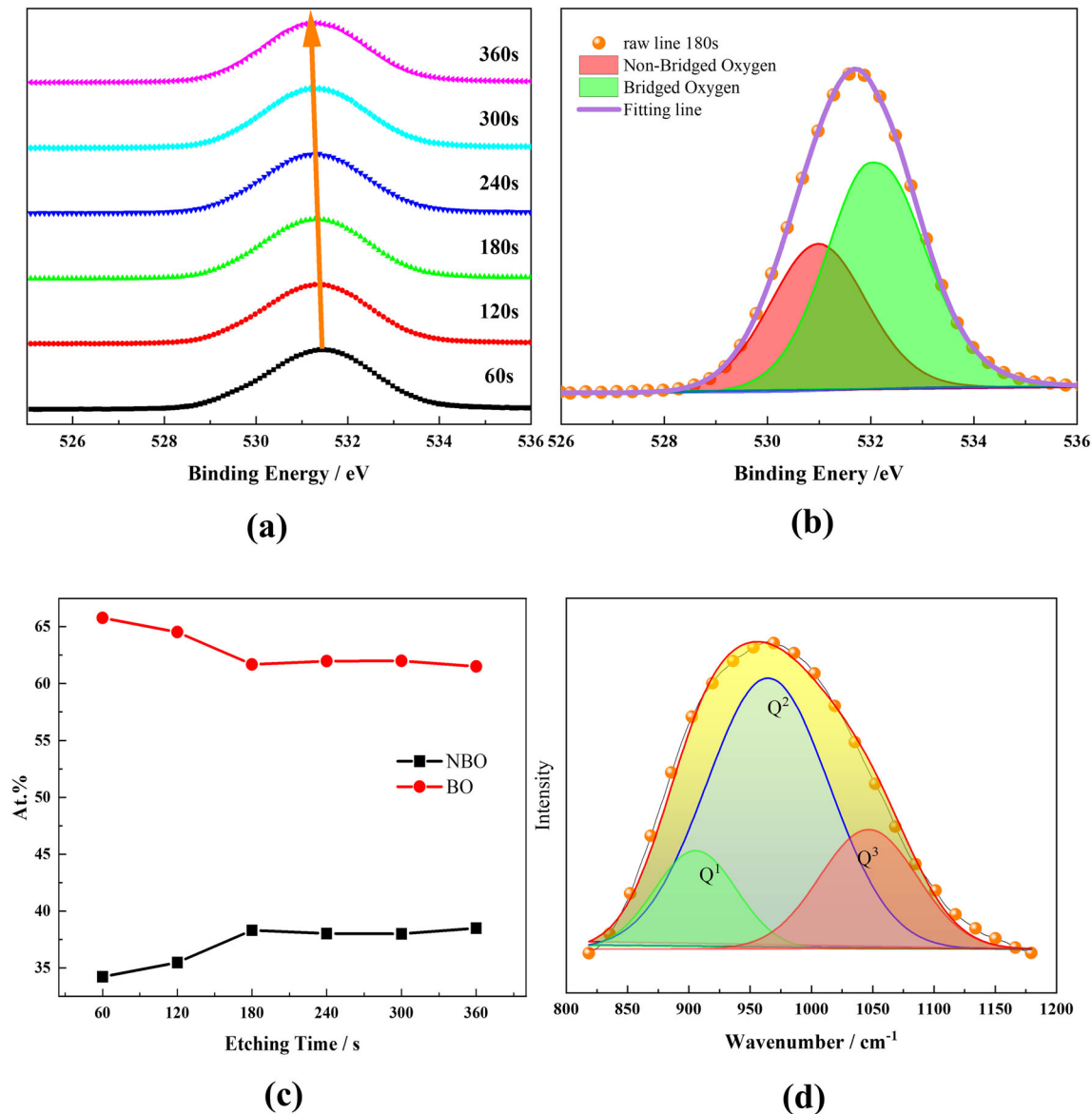| Reaction	$\Delta G°$ (J/mol)
[Fe] + (MnO) = (FeO) + [Mn]	94,182.8
[Fe] + 1/2(SiO_2) = (FeO) + 1/2[Si]	139,972.2
CaS(l) + MnO(l) = MnS(l) + CaO(l)	28,699.7
MnS(l) + FeO(l) = FeS(l) + MnO(l)	5800.8

Fig. 6—(a) O1s spectrum for different etching time; (b) typical O1s fitting results at 180 s; (c) quantitative results of O1s spectra at different etching time; (d) Raman results of the slag bulk.

In order to obtain the structure of the body, the crushed slag was subjected to Raman test. The literature[50–53] show that the bands at about ~ 870, ~ 910, ~ 960, and ~ 1050 cm^{-1} can be assigned to Q^0(SiO$_4^{4-}$), Q^1(Si$_2$O$_7^{6-}$), Q^2(Si$_2$O$_6^{4-}$), Q^3(Si$_2$O$_5^{2-}$). The fitting results are shown in Figure 6(d) and Table V. The results show that the Q^2 structural unit in the bulk is the main component, accounting for about 62.80 pct, while Q^1 and Q^3 account for 15.02 and 22.18 pct, respectively. The results of the Raman fits for different basicity are shown in Figure S6 in supplementary material and Table V. As basicity increases from 0.5 to 1.2, Q^0 and Q^1 increase to 11.99 and 49.23 pct, Q^2 and Q^3 decrease to 28.90 and 9.88 pct respectively. The structure of the body gradually depolymerises with increasing basicity. The schematic diagram of the bulk structure is shown in Figure 7(a). The structure of the body is mainly composed of chain and reticulated silicate structure. To analyze the difference between the slag–metal interfacial structure and the body, the XPS results are compared with computed results using the cell model,[54] as shown in Figure 7(b). Combined with structural analysis, as shown in the figure, the interface structure will deviate from the bulk structure, but gradually converge to the bulk with increasing depth, the structure at 360 seconds is essentially the same as the body structure.

Traditionally, Sulfur first undergoes an exchange reaction with free oxygen at the interface, as shown in Eq. [3]. However, previous studies[11] in our group have shown that not only free oxygen can absorb and remove

Sulfur atoms, but also non-bridging oxygen can do. Due to a large number of electrons around the Fe, Mn transition elements, their charge effect acts with oxygen and completes the absorption of sulfur. As the content of NBO at the interface gradually increases with depth, so does the Sulfur, which is in good agreement with its distribution. After entering the slag, Sulfur will combine with Fe, Mn and other metal cations to form stable sulfides[10,11] and accumulate in the interfacial boundary layer. To further reveal the physicochemical reactions occurring at the interface, further analysis is carried out in conjunction with the oxidation of iron and the removal of sulfur, as follows.

Firstly, the sulfur removal and iron oxidation reactions are Eqs. [1], [2] and [3]. The conversion reaction of the three types of oxygen in the slag is

$$2(O^-) = (O^{2-}) + (O^0) \qquad [4]$$
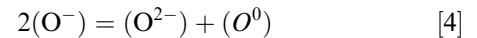
where O$^-$ is NBO (Si–O–M, M = Fe, Mn), O^{2-} is free oxygen and O^0 is BO (Si–O–Si). Based on experimental results, there is almost no free oxygen in the slag, thus combining Eqs. [3] and [4], the desulfurization reaction for this system can be written as

$$[S] + 2(O^-) = [O] + (O^0) + (S^{2-}) \qquad [5]$$

Therefore, the total reaction of desulfurization and oxidation can be written as

$$[S] + 2(O^-) + [Fe] + (Mn^{2+}) = [O] + (O^0) + (FeS) + [Mn] \qquad [6]$$

$$[S] + 2(O^-) + [Fe] + 1/2(Si^{4+}) = [O] + (O^0) + (FeS) + 1/2[Si] \qquad [7]$$
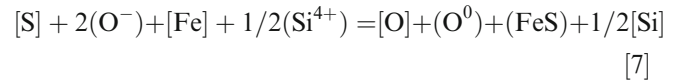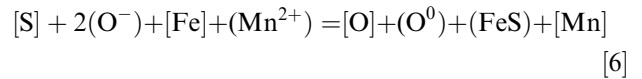
Table V. Fitting Quantitative Results of Raman Spectra

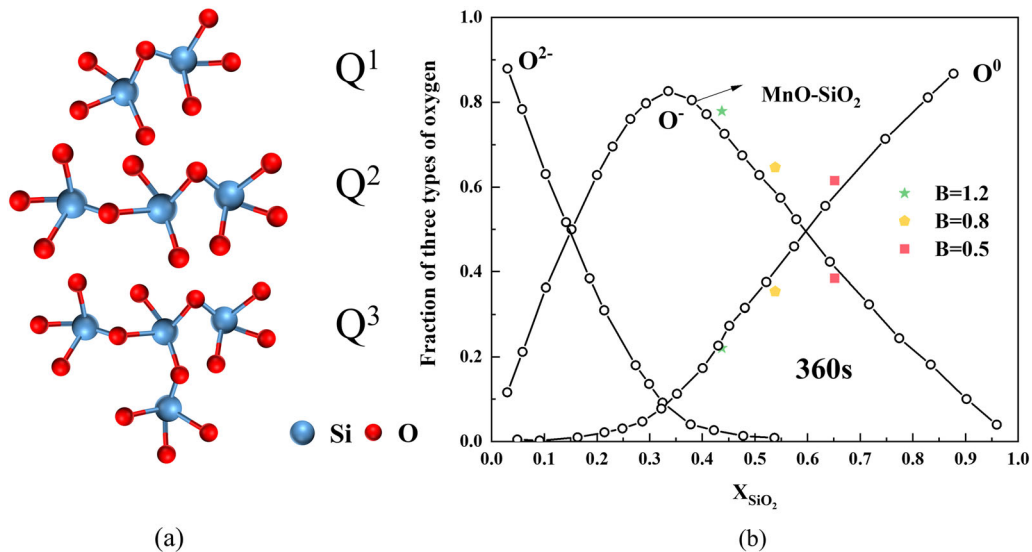| Samples	Q^3 (Pct)	Q^2 (Pct)	Q^1 (Pct)	Q^0 (Pct)
Slag-A	22.18	62.80	15.02	0
Slag-B	12.2	41.68	43.41	2.71
Slag-C	9.88	28.90	49.23	11.99

Fig. 7—(a) Schematic diagram of Raman results of the slag bulk; (b) comparison of simple bulk structure model and XPS results.
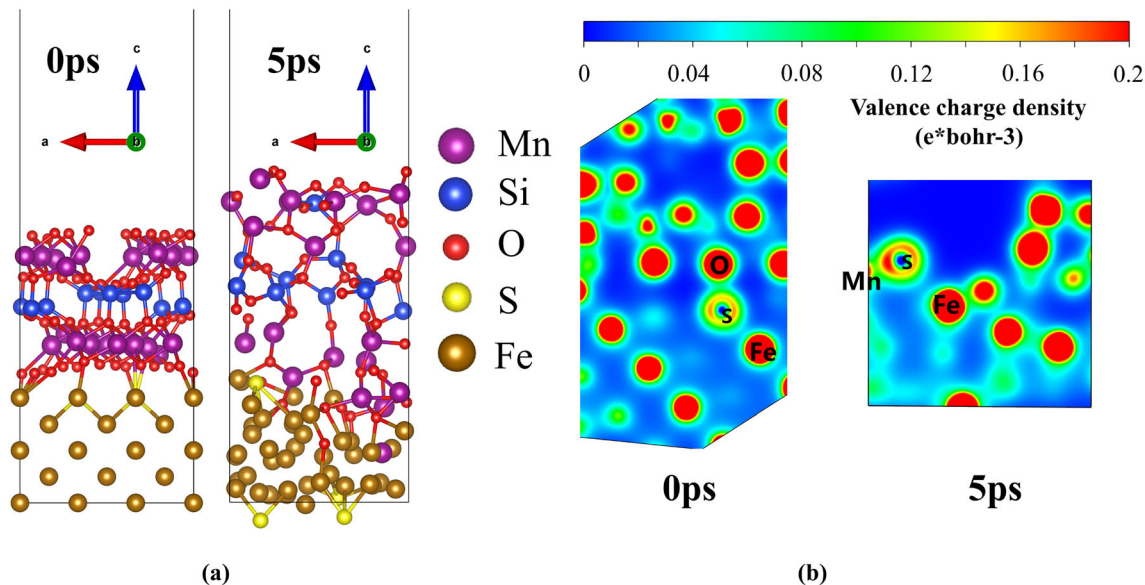
Fig. 8—(a) Snapshot before and after melting (0 and 5 ps); (b) interfacial charge distribution before and after melting (0 and 5 ps).

The total reaction shows that FeS and BO are present at the interface of the slag, and the results of this experiment give consistent proof.

C. Computational Simulation of the Slag–Metal Interface Based on the First Principle

In order to elucidate the slag–metal interaction mechanism, the slag–metal interface was simulated using the AIMD method, and the elemental distribution and charge valence of the interface were extracted and analysed after completion of the calculation.

Figure 8(a) shows a snapshot of the slag–metal interface before and after melting and it can be seen that at 0 ps, S is distributed at the slag–metal interface and the oxygen termination layer is in contact with the metal. After melting at 1600 °C for 5 ps, the metal liquid and slag system becomes disordered, some of the O and Mn atoms in the slag enter the ferric metal liquid and some of the original Fe atoms are connected to oxygen, this phenomenon proves the reduction of Mn at the slag–metal interface and the oxidation of Fe, *i.e.* the reaction Eq. [1]. For the distribution of sulfur atoms, as sulfur is an interfacially active element, some of the sulfur atoms migrate to a stable presence at the interface between the metal liquid and the vacuum layer, while one sulfur atom is absorbed at the slag–metal interface and is linked to the Fe and Mn atoms. And due to the size limitations of the system, the absorption of one sulfur atom by the slag under this condition already results in a high sulfur content in the slag and therefore may not be able to absorb any more sulfur atoms, resulting in their migration to the metal-vacuum interface. Figure 8(b) shows the charge distribution before and after melting. It can be clearly seen that there is very little charge around the sulfur and the charge is mainly concentrated around the oxygen and the transition metals Mn or Fe. At 0 ps, the sulfur and oxygen at the

interface are in contact, at which point the charge distribution of S has a regular spherical shape, indicating the uniformity of its charge distribution. At 5 ps after melting, the sulfur undergoes an interfacial reaction at the interface, where the sulfur is mainly linked to Fe and Mn. At this point, the charge distribution of sulfur becomes spindle-shaped, with the charge predominantly biased towards Mn, further indicating that MnS is more stable than FeS, and therefore FeS at the interface is transferred to MnS, which is in good agreement with the experiment. In order to quantify the interfacial reaction process, the valence state of each interfacial atom is analysed.

Figure 9 shows the valence distribution of each atom before and after melting, while the specific valence states of the atoms at the slag–metal interface are listed in Table VI. A comparison of (a) and (b) in Figure 9 and Table VI shows that the valence state of interfacial Fe will partially increase, the valence states of Mn and S will decrease and the valence state of oxygen is decreasing. The change in valence of Fe and Mn indicates a redox reaction at the interface, while the valence of sulfur is decreasing, indicating an oxidative removal process of sulfur, and the oxygen portion of the interface is increasing, due to the oxidation of metallic iron which results in some of the charge of iron giving O and therefore an increase in the oxygen valence. Thus, the calculations provide further evidence for the two reactions postulated in the previous section in terms of valence and charge, and are in good agreement with the experimental results.

Therefore, combined with the experimental and simulation results, the slag–metal interface is schematically shown in Figure 10. In the slag–metal interface, two interfacial chemical reactions occur at the interface, one is the oxidation of the metal and the other is the dissolution and removal of Sulfur. As shown in Eqs. [6] and [7], interfacial reactions lead to an increase in BO in
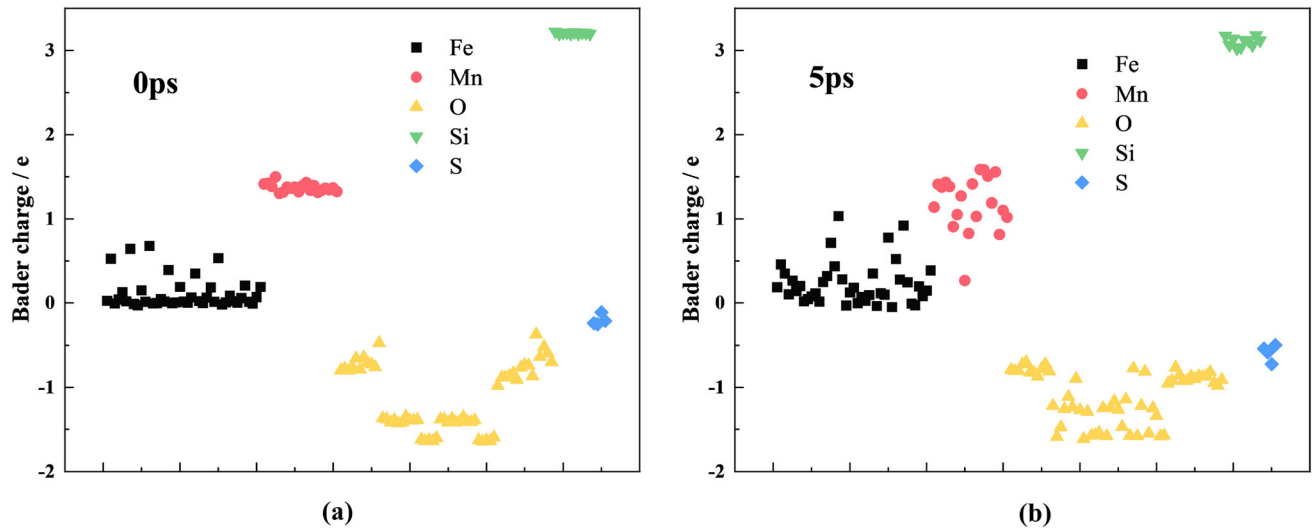
Fig. 9—(a) Bader valence charge at 0 ps; (b) Bader valence charge at 5 ps.

Table VI. Bader Charge Distribution of Interface Atoms

| Atoms	0 ps	5 ps	Atoms	0 ps	5 ps
S1	− 0.24137	− 0.5388	Mn20	1.32048	1.01941
S2	− 0.25483	− 0.5852	O42	− 0.98149	− 0.95499
S3	− 0.11202	− 0.72243	O43	− 0.88407	− 0.91933
S4	− 0.21278	− 0.49665	O44	− 0.88161	− 0.76312
Fe2	0.52736	0.45901	O45	− 0.86369	− 0.86036
Fe7	0.64588	0.20507	O46	− 0.8317	− 0.92171
Fe12	0.68047	0.01551	O47	− 0.91123	− 0.92011
Fe17	0.39238	1.03394	O48	− 0.76457	− 0.87084
Fe30	0.53417	0.77864	O49	− 0.73292	− 0.90053
Mn6	1.31509	0.90632	O50	− 0.73939	− 0.86571
Mn7	1.37395	1.04962	O51	− 0.86733	− 0.87387
Mn8	1.36043	1.26893	O52	− 0.37249	− 0.86292
Mn9	1.37348	0.26557	O53	− 0.63736	− 0.81809
Mn10	1.31702	0.82741	O54	− 0.51935	− 0.94862
Mn17	1.36034	1.55325	O55	− 0.59206	− 0.97818
Mn18	1.34344	0.81262	O55	− 0.69888	− 0.90982
Mn19	1.36482	1.10078			
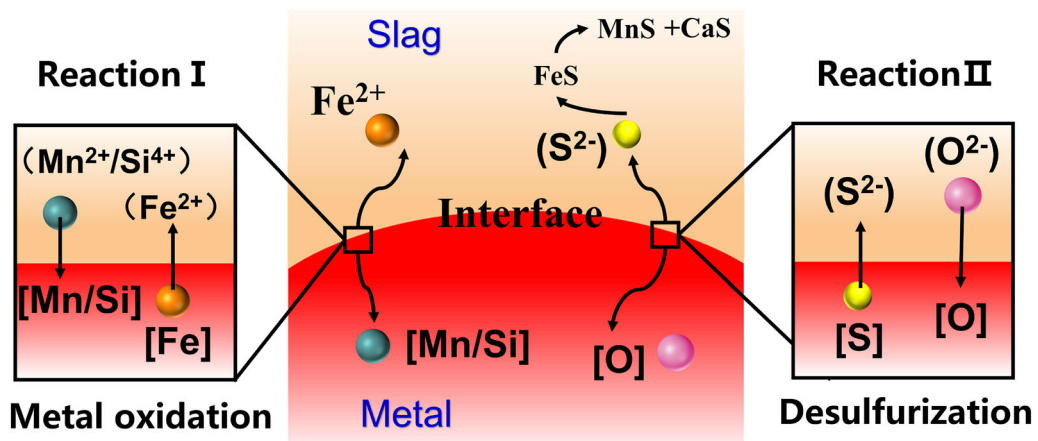
Fig. 10—Schematic diagram of slag–metal interface.

the slag–metal interface. Instantaneous contact of the slag and metal leads to the oxidation of Fe and the formation of Fe–O at the interface, as shown by the XPS results. The gradual increase of Mn and O with depth and the presence of Fe divalent confirm the occurrence of redox reactions of Fe and Mn. Afterward, FeO can be used as a carrier for the desulfurization reaction. The distribution of Sulfur on the slag side confirms the occurrence of Sulfur dissolution reactions, then Sulfur migrates around elements such as Fe and Mn resulting in the Fe–S and Mn–S appearing to aggregate in the interfacial layer. The presence of FeO and the generation of BO during the desulfurization process both lead to an increase in the interfacial oxygen potential. Therefore, more BO and less NBO are present at the interface. The method initially characterizes the structure and elemental distribution of the slag–metal interface, and also further confirms the existence of physicochemical reactions between the slag–metal interface, laying the foundation for future studies on the physicochemical properties of the slag–metal interface.

IV. CONCLUSIONS

This study proposed a method to directly characterize the elemental distribution and structure of the slag–metal interface and revealed the limiting aspects of desulfurization at the slag–metal interface. In this paper, the interfacial properties between the MnO-based slag system and the sulfur-containing liquid metal were characterized using XPS etching. The results show that the relative content of Si and O gradually decreases with depth and that of Ca, Mn and S increases as the etching depth increases. Meanwhile, Mn exists in positive divalent form, S in negative divalent form, and Fe in both Fe–O and Fe–S forms. For the slag–metal interface structure, the BO gradually decreases and the NBO gradually increases as depth deepens. With increasing basicity, the interfacial BO gradually decreases and the NBO gradually increases. The increase in basicity leads to a faster diffusion of sulfur and therefore to a decrease in Fe–S at the interface. Based on the above experimental and simulation results, two interfacial chemical reactions are proposed. One is an oxidation reaction of Fe with Mn/Si in slag. The other is the exchange reaction between sulfur and oxygen, resulting in the dissolution of sulfur. Then, Sulfur will form stable sulfides with metal elements such as Mn and Ca and aggregate at the slag–metal interface.

CONFLICT OF INTEREST

On behalf of all authors, the corresponding author states that there is no conflict of interest.

SUPPLEMENTARY INFORMATION

The online version contains supplementary material available at https://doi.org/10.1007/s11663-023-02759-8.

REFERENCES

1. K. Steneholm, N.A.I. Andersson, A. Tilliander, and P.G. Jonsson: *Ironmak. Steelmak.*, 2018, vol. 45, pp. 114–24.
2. G.R. Belton, T.J. Evans, and L. Strezov: *Philos. Trans. R. Soc. A*, 1998, vol. 356, pp. 941–53.
3. M.A. Rhamdhani, K.S. Coley, and G.A. Brooks: *Metall. Mater. Trans. B Process Metall. Mater. Process. Sci.*, 2005, vol. 36B, pp. 591–604.
4. M. Radune, D. Ophir, A. Lugovskoy, M. Zinigrad, and D. Eliezer: in *Defect and Diffusion Forum*, Trans Tech Publications, 2006, pp. 433–40.
5. C.J.B. Fincham and F.D. Richardson: *Proc. R. Soc. Lond. Ser. A Math. Phys. Sci.*, 1954, vol. 223, pp. 40–62.
6. K.C. Mills, M. Hayashi, L. Wang, and T. Watanabe: in *Treatise on Process Metallurgy*, ed. S. Seetharaman, Elsevier, Boston, 2014, pp. 149–286.
7. J.-H. Park and P.C.-H. Rhee: *J. Non-Cryst. Solids*, 2001, vol. 282, pp. 7–14.
8. L. Wang, Y. Wang, Qi. Wang, and K. Chou: *Metall. Mater. Trans. B.*, 2016, vol. 47B, pp. 10–15.
9. Y.-B. Kang and J.H. Park: *Metall. Mater. Trans B* 2011, vol. 42B, pp. 1211–17.
10. X. He, S. Ma, L. Wang, H. Dong, and K. Chou: *Metall. Mater. Trans. B.*, 2021, vol. 52B, pp. 3346–53.
11. X. He, S. Ma, L. Wang, H. Dong, and K. Chou: *J. Alloys Compd.*, 2022, vol. 896, 163008.
12. I. Egry and J. Brillo: *J. Chem. Eng. Data*, 2009, vol. 54, pp. 2347–52.
13. J. Choe, H.G. Kim, Y. Jeon, H.J. Park, Y. Kang, S. Ozawa, and J. Lee:*ISIJ Int.*, 2014, vol. 54, pp. 2104–08.
14. W. Cao, L. Muhmood, and S. Seetharaman: *Metall. Mater. Trans. B*, 2011, vol. 43B, pp. 363–69.
15. T. Matsushita, I. Belov, D. Siafakas, A.E.W. Jarfors, and M. Watanabe: *J. Mater. Sci.*, 2021, vol. 56, pp. 7811–22.
16. K. Gu, N. Dogan, and K.S. Coley:*Metall. Mater. Trans. B*, 2017, vol. 48B, pp. 2343-53.
17. K. Gu, N. Dogan, and K.S. Coley: *Metall. Mater. Trans. B.*, 2017, vol. 48B, pp. 2984–3001.
18. P.Y. Ni, T. Tanaka, M. Suzuki, M. Nakamo, and P.G. Jonsson: *ISIJ Int.*, 2018, vol. 58, pp. 1979–88.
19. P. Ni, T. Tanaka, M. Suzuki, M. Nakamoto, and P.G. Jönsson: *ISIJ Int.*, 2019, vol. 59, pp. 737–48.
20. X.B. He, L.J. Wang, and K.C. Chou: *Ceram. Int.*, 2021, vol. 47, pp. 12476–82.
21. X. He, L. Wang, and K. Chou: *J. Alloys Compd.*, 2021, vol. 876, 160209.
22. J. Yang, Z. Wang, and Il. Sohn: *Acta Mater.*, 2022, vol. 234, 118014.
23. S. Niu, Z. Yang, Y. Wang, and D. Wang: *Appl. Surf. Sci.*, 2022, vol. 576, p. 151878.
24. V. Turlo, O. Politano, and F. Baras: *Acta Mater.*, 2015, vol. 99, pp. 363–72.

25. W. Fu, X. Wang, J. Zhou, and Y. Yu: *Comput. Mater. Sci.*, 2022, vol. 211, p. 111546.
26. G. Kresse and J. Furhmuller: *Phys. Rev. B*, 1993, vol. 47, p. R558.
27. G. Kresse and J. Furthmüller: *Phys. Rev. B*, 1996, vol. 54, p. 169.
28. P.E. Blöchl: *Phys. Rev. B*, 1994, vol. 50, p. 17953.
29. J.P. Perdew, K. Burke, and M. Ernzerhof: *Phys. Rev. Lett.*, 1996, vol. 77, pp. 3865–68.
30. R. Wendy and D.T. Griffen: *Am. Mineral.*, 2005, vol. 90, pp. 969–83.
31. V. Wang, N. Xu, J.C. Liu, G. Tang, and W.T. Geng: arXiv preprint, 2019, arXiv:1908.08269.
32. K. Momma and F. Izumi: *J. Appl. Crystallogr.*, 2011, vol. 44, pp. 1272–76.
33. V. Di Castro and G. Polzonetti: *J. Electron. Spectrosc. Relat. Phenom.*, 1989, vol. 48, pp. 117–23.
34. M.C. Biesinger, B.P. Payne, A.P. Grosvenor, L.W.M. Lau, A.R. Gerson, and R.S. Smart: *Appl. Surf. Sci.*, 2011, vol. 257, pp. 2717–30.
35. E.S. Ilton, J.E. Post, P.J. Heaney, F.T. Ling, and S.N. Kerisit: *Appl. Surf. Sci.*, 2016, vol. 366, pp. 475–85.
36. I. Uhlig, R. Szargan, H.W. Nesbitt, and K. Laajalehto: *Appl. Surf. Sci.*, 2001, vol. 179, pp. 222–29.
37. S. Boursiquot, M. Mullet, and J.-J. Ehrhardt: *Surf. Interface Anal.*, 2002, vol. 34, pp. 293–97.
38. W.M. Skinner, H.W. Nesbitt, and A.R. Pratt: *Geochim. Cosmochim. Acta*, 2004, vol. 68, pp. 2259–63.
39. Q. Xiang, S. Li, X.F. Zou, Y.J. Qiang, B.B. Hu, Y. Cen, C.L. Xu, L.J. Liu, Y. Zhou, and C.G. Chen: *Appl. Surf. Sci.*, 2018, vol. 462, pp. 65–72.
40. M.D. Walle, K. Zeng, M. Zhang, Y. Li, Y.N. Liu, *Appl. Surf. Sci.* 2019, vol. 473, pp. 540–47.
41. Y. Chang, F. Hong, C. He, Q. Zhang, and J. Liu: *Adv. Mater.*, 2013, vol. 25, pp. 4794–99.
42. L.J. Wang, M. Hayashi, K.C. Chou, and S. Seetharaman: *Metall. Mater. Trans. B*, 2012, vol. 43B, pp. 1338–43.
43. J.H. Park and G.-H. Park: *ISIJ Int.*, 2012, vol. 52, pp. 764–69.
44. Y. Park and D.J. Min: *ISIJ Int.*, 2016, vol. 56, pp. 520–26.
45. L. Muhmood, N,N. Viswanathan, and S. Seetharaman: in *Ninth International Conference on Molten Slags, Fluxes and Salts (MOLTEN12)*.
46. J.H. Park and P.C.H. Rhee: *J. Non-Cryst. Solids*, 2001, vol. 282, pp. 7–14.
47. H. Kim and Il. Sohn: *ISIJ Int.*, 2011, vol. 51, pp. 1–8.
48. L. Wang, Yu. Jipeng, K. Chou, and S. Seetharaman: *Metall. Mater. Trans. B.*, 2015, vol. 46B, pp. 1802–08.
49. X. He, L. Wang, and K.-C. Chou: *Metall. Mater. Trans. B*, 2022, vol. 53, pp. 1583–92.
50. W. Dean, S.K. Sharma, and J.A. Philpotts: *J. Non-Cryst. Solids*, 1983, vol. 58, pp. 323–52.
51. Y. Iguchi, S. Kashio, T. Goto, Y. Nishina, and T. Fuwa: *Can. Metall. Q.*, 1981, vol. 20, pp. 51–56.
52. Y. Tsunawaki, N. Iwamoto, T. Hattori, and A. Mitsuishi: *J. Non-Cryst. Solids*, 1981, vol. 44, pp. 369–78.
53. B. O. Mysen, D. Virgo, and C.M. Scarfe: *Am. Mineral.*, 1980, vol. 65, pp. 690–710.
54. L. Zhang and S. Jahanshahi: *Metall. Mater. Trans. B.*, 1998, vol. 29B, pp. 177–86.